The plateau phase of gamma-ray burst afterglows in the thick-shell scenario

Leventis, K.; Wijers, R.A.M.J.; van der Horst, A.J.

Published in:
Monthly Notices of the Royal Astronomical Society

DOI:
10.1093/mnras/stt2055

Monthly Notices
of the
ROYAL ASTRONOMICAL SOCIETY

MNRAS **437,** 2448–2460 (2014)
Advance Access publication 2013 November 26

doi:10.1093/mnras/stt2055

The plateau phase of gamma-ray burst afterglows in the thick-shell scenario

K. Leventis,* R. A. M. J. Wijers and A. J. van der Horst

Astronomical Institute 'Anton Pannekoek', PO Box 94248, NL-1090 SJ Amsterdam, the Netherlands

Accepted 2013 October 23. Received 2013 September 30; in original form 2013 January 22

ABSTRACT

We present analytic calculations of synchrotron radiation from the forward and the reverse shock of gamma-ray burst blast waves, in the thick-shell scenario (i.e. when the reverse shock is relativistic). We show that this scenario can naturally account for the plateau phase, observed early in the afterglows of about half the bursts detected by *Swift*. We generalize our approach to include power-law luminosity of the central engine and show that when radiation from both regions (forward and reverse shock) is taken into account, a wide range of possibilities emerge, including chromatic and achromatic breaks, frequency-dependent spectral evolution during the injection break and widely varying decay indices in different bands. For both the forward and the reverse shock, we derive formulas for the spectral parameters and the observed flux in different power-law segments of the spectrum, as a function of observer time. We explore the $F_{\rm b}-t_{\rm b}$ relation (between the observed time of the end of the plateau phase and the flux at that point) in the framework of the presented model and show that model predictions favour the reverse shock as the dominant source of emission in both optical and X-rays. As case studies, we present simultaneous fits to X-ray and optical/IR afterglow data of GRB 080928 and GRB 090423. We identify the end of the plateau phase with the cessation of energy injection and infer the corresponding upper limits to central-engine activity, which are about 1 h for the former and 1.5 h for the latter. We conclude that smooth energy injection through the reverse shock is a plausible explanation for the plateau phase of gamma-ray burst afterglows. During that phase, radiation from the reverse shock is likely to be important, or even dominant, and should be taken into account when fitting model parameters to observations.

Key words: hydrodynamics – radiation mechanisms: non-thermal – relativistic processes – shock waves – methods: analytical – gamma-ray burst: general.

1 INTRODUCTION

The afterglow radiation of gamma-ray bursts (GRBs) carries important diagnostics of the physics behind these events. The most recent advances in the study of afterglows have been initiated by observations of the *Swift* satellite (Gehrels et al. 2005). Perhaps the most intriguing discovery of *Swift* has been the afterglow behaviour within the first few hours after the burst (Nousek et al. 2006; Zhang et al. 2006). X-ray and optical light curves during that period reveal the details of the transition from the prompt emission, responsible for the gamma-rays, to the canonical afterglow behaviour, typically attributed to synchrotron radiation from an adiabatic relativistic blast wave (see Mészáros 2006 for a review). This transition, however, has been found to be rich in features that cannot be explained by the classic fireball model. These features include flares, plateaus, chromatic and achromatic breaks and different decay indices than those observed at time-scales of days to weeks.

Regular features in *Swift* data, flares and plateaus have often been linked to delayed or prolonged engine activity (Nousek et al. 2006; Panaitescu et al. 2006a; Zhang et al. 2006). In the case of flares, the energy supply is episodic and, similarly to the origin of the prompt emission, results in internal dissipation of the kinetic energy. In the case of plateaus, the energy supply is gradual, leading to smoother light curves. The energy is 'injected' into the blast wave through the reverse shock (RS) which propagates inside the ejecta. If long-lasting, energy injection can have important consequences on the dynamics by introducing an intermediate phase during which the deceleration of the blast wave is moderated by the rate of energy supply (Sari & Piran 1995). This is what is known as the 'thick-shell' scenario.

Calculations of the spectral signatures of the RS, usually assuming synchrotron radiation, have been used to predict or interpret the irregular behaviour in radio, optical and X-ray frequencies (Panaitescu, Meszaros & Rees 1998; Sari & Piran 1999; Kobayashi

* E-mail: K.N.Leventis@gmail.com

& Sari 2000; Kumar & Panaitescu 2003; Zhang et al. 2006; Uhm & Beloborodov 2007; Dall'Osso et al. 2011; Panaitescu & Vestrand 2012). However, these studies are mostly concerned with non-relativistic RS, and when the relativistic phase is addressed, radiation from the RS is either ignored or calculated only after the RS has crossed the ejecta (see however Nakar & Piran 2004, and Uhm 2011 and Uhm et al. 2012 for a treatment of mildly relativistic RS). But if the plateau phase of the afterglow indeed reflects energy injection, the inferred duration (10^3–10^5 s) can easily result in a relativistic RS which may contribute significantly to the observed radiation, during the entire plateau phase.

Understanding the effects of prolonged energy injection and the resulting radiation from the forward shock (FS) and the RS is important for two main reasons. The first reason is that the profile of the ejecta, probed through afterglow observations, carries important information on the ejection mechanism of the central object (and thus its identity) and especially on the processes that modify that profile during the prompt emission. The second reason is that early-afterglow data have blurred the picture regarding the existence and time of jet breaks in GRB afterglows, partially due to their similarity to injection breaks (Racusin et al. 2009). Therefore, separation of the two effects is crucial to infer reliably the jet properties and thus the correct energetics of these events.

In this work, we use a simple analytic description of the dynamics of the blast wave while the RS is relativistic and track the radiation both from the FS and the RS self-consistently. Once all the ejected particles have been shocked, the dynamics settles into the adiabatic phase, the transition manifested as a simultaneous break in light curves of different bands. This is the so-called injection break, after which radiation from the RS fades quickly due to expansion and radiative losses. By exploring reasonable values for the physical parameters, we show that a range of possibilities exist for the observed spectra, during the intermediate phase, but also at the time of the injection break.

At this point, we consider it useful to define some terms we will be using throughout this paper and briefly discuss the ambiguity in the use of the word '(a)chromatic', common nomenclature of the field. In Harrison et al. (1999), where for the first time a simultaneous steepening of the afterglow light curves was interpreted as evidence for the presence of a jet in GRB 990510, the optical break is characterized as 'achromatic' due to the lack of spectral evolution locally (i.e. in optical bands). However, in most of the subsequent publications (e.g. Granot & Loeb 2001; Panaitescu et al. 2006b; Li et al. 2012), '(a)chromatic' is used to mean 'frequency-(in)dependent' rather than '(not) accompanied by spectral evolution'. In this paper, we will be concerned both with temporal breaks occurring at only one frequency and with temporal breaks accompanied by spectral evolution locally, regardless of the possible simultaneity of breaks at other frequencies. We will use the word 'chromatic' to refer to light-curve breaks that are not accompanied by breaks at other frequencies, while 'achromatic' will be the breaks that occur simultaneously at two or more frequencies, regardless of the temporal indices before and after the break. When the spectrum changes locally (i.e. around an observing frequency) during a temporal break, we will refer to it as 'change of the spectral index', or simply 'spectral evolution'.

This paper is structured as follows. In Section 2, we present our description of the dynamics, radiation and particle populations of both the FS and the RS, in the case of steady energy injection. We also generalize our approach to energy injection that can be described by a power law in time. In Section 3, we show a direct numerical implementation of the model and discuss the richness of the resulting light curves as a consequence of the interplay between FS and RS radiation. In Section 4, we present formulas for the spectral parameters and the observed flux from both radiating regions. In Section 5, we present eyeball fits of model light curves to both X-ray and optical data of two afterglows with a plateau phase. In Section 6, we discuss our results in the context of early afterglow observations and assess the feasibility of the thick-shell scenario as an interpretation of the observations. We conclude by summarizing our main findings in Section 7.

2 MODEL

In this section, we present a detailed derivation of the dynamics and spectral parameters during energy injection. For the adiabatic phase that follows after the injection break, see, for example, Sari, Piran & Narayan (1998). The first part of the calculations is concerned with the characteristic time-scales of the model. Such calculations have been presented in the past in various different forms, but we repeat them here for completeness, but also as a reference for the subsequent analysis.

The main assumptions are those of a single-zone approximation both for the shocked ejecta and for shocked circumburst medium (CBM), pressure equilibrium at the contact discontinuity (CD) separating the two, and a thin-zone approximation, where we neglect differences in the arrival times of photons emitted simultaneously (in the lab frame) but at different depths inside the blast wave. For simplicity, the density distribution of the CBM is taken to be homogeneous.

2.1 Dynamics and time-scales of thick shells

We assume a constant ejection of mass from the central source with Lorentz factor η. The duration of the ejection is Δt in the lab frame. The total energy of the ejecta is initially purely kinetic (cold ejecta) and is denoted by E, while the CBM is assumed to have a constant density n_1. The four physical parameters η, Δt, E and n_1 uniquely determine the dynamical evolution of the blast wave that is generated as the ejecta plough into the CBM.

There are four regions in this scenario. Region 1 is the unshocked CBM, while region 2 is the CBM that has been shocked by the FS. Region 3 contains the ejecta that have been shocked by the RS and region 4 the unshocked ejecta. Regions 2 and 3 are the only ones that produce radiation as a result of converting part of the kinetic energy of the ejecta to thermal energy, via the FS and the RS. Subscripts 1, 2, 3 and 4 will be used throughout this paper to specify the region that a quantity refers to.

The pressure in regions 2 (shocked CBM) and 3 (shocked ejecta) can be approximated by (see Beloborodov & Uhm 2006)

$$P_2 = \frac{e_2}{3} = \frac{4}{3}\,\gamma_2^2\, m_{\rm p}\, n_1\, c^2 \tag{1}$$

$$P_3 = \frac{e_3}{3} = \frac{4}{3}\,\left(\gamma_{34}^2 - 1\right)\, m_{\rm p}\, n_4'\, c^2, \tag{2}$$

where γ_2 is the Lorentz factor of region 2 in the lab frame and γ_{34} is the relative Lorentz factor between regions 3 and 4. The quantity $n_4' = n_4/\eta$ is the number density of particles in region 4 in its comoving frame. Focusing for now our attention on spherical outflows, conservation of mass implies

$$n_4 = \frac{E}{4\,\pi\, m_{\rm p}\, c^5\, \eta\, \Delta t}\, t_{\rm lab}^{-2}. \tag{3}$$

Demanding pressure equilibrium at the CD between regions 2 and 3, we see that the ratio $f = n'_4/n_1 = \gamma_2^2/(\gamma_{34}^2 - 1)$ decreases with time and therefore the initially Newtonian RS becomes faster until it becomes relativistic. That happens when $\gamma_{34}^2 = 2$ (corresponds to $\gamma_{34}\beta_{34} = 1$, i.e. the spatial component of the RS's four-velocity, as measured in the frame of region 4, is c). As time passes, the RS will eventually become ultrarelativistic. Then, by further assuming that $\gamma_2 = \gamma_3$ (i.e. regions 2 and 3 are comoving), we can write

$$\gamma_{34}\,\gamma_2 \approx \frac{\eta}{2}. \tag{4}$$

However, this relation is not valid at the transition, when $\gamma_{34} = \sqrt{2}$. To also account for that phase, we propose the following relation which satisfies pressure equilibrium throughout the intermediate dynamical regime and shows the correct asymptotic behaviour

$$\left(\gamma_{34}^2 - 1\right)^{1/2}\,\gamma_2 \approx \frac{\eta}{2}. \tag{5}$$

From equation (5), we find that the RS becomes relativistic when $f = \eta^2/4$. The lab-frame time at which this occurs is

$$t_{\rm rel} = \left(\frac{E}{\pi\, m_{\rm p}\, c^5\, n_1\, \eta^4\, \Delta t}\right)^{1/2}. \tag{6}$$

This time-scale ($t_{\rm rel}$) should be compared against the lab-frame time it takes the FS to give half the blast-wave energy to the CBM:

$$t_{\rm CBM} = \left(\frac{3\,E}{8\pi\, m_{\rm p}\, c^5\, n_1\, \eta^2}\right)^{1/3}. \tag{7}$$

If $t_{\rm CBM} < t_{\rm rel}$, the outflow will enter the Blandford–McKee self-similar phase (Blandford & McKee 1976) before the RS becomes relativistic. However, if $t_{\rm CBM} > t_{\rm rel}$, the RS will first become relativistic. This is, in fact, the condition for the thick-shell scenario (see, for example, Sari & Piran 1995).

It is straightforward to express the Lorentz factors of the two shocks as a function of time, once the RS has become relativistic:

$$\gamma_2 = \frac{\eta}{2}\left(\frac{t_{\rm rel}}{t_{\rm lab}}\right)^{1/2} \tag{8}$$

$$\gamma_{34} = \left[\left(\frac{\eta}{2\gamma_2}\right)^2 + 1\right]^{1/2}. \tag{9}$$

This phase will end when the FS becomes non-relativistic or the RS crosses the shell of ejecta, whichever comes first. The lab-frame time of the FS becoming non-relativistic can be found using equation (8) for a final Lorentz factor of $\sqrt{2}$,

$$t_{\rm newt} = \frac{\eta^2\, t_{\rm rel}}{8}. \tag{10}$$

The lab-frame time at which the RS crosses the shell can be found by simply considering the lab-frame width of the shell and the difference in lab-frame velocity between the unshocked ejecta and the shocked ejecta, once the RS has become relativistic,

$$c\,\Delta t = \int_0^{t_{\rm cr}} (v_{\rm ej} - v_2)\,{\rm d}t_{\rm lab} \approx \frac{c}{2}\int_0^{t_{\rm cr}} \left(\frac{1}{\gamma_2^2} - \frac{1}{\eta^2}\right)\,{\rm d}t_{\rm lab}. \tag{11}$$

Using the approximation $\eta \gg \gamma_2$ and expressing γ_2 through equation (8), we find

$$t_{\rm cr} \approx \eta\,(t_{\rm rel}\,\Delta t)^{1/2}. \tag{12}$$

A useful consistency check here is to note that we get the same result when calculating the lab-frame time at which the FS has given half of the blast-wave energy to the CBM according to the scaling presented in equation (8).

The observed time-scales can be found by using the well-known formula resulting from the finite speed of light:

$${\rm d}t_{\rm obs} = \frac{{\rm d}t_{\rm lab}}{2\,\gamma_2^2} \tag{13}$$

and integrating through the appropriate time interval. In this way we find

$$t_{\rm rel,obs} = \frac{2\,t_{\rm rel}}{\eta^2} \tag{14}$$

and

$$t_{\rm cr,obs} = \Delta t + \frac{t_{\rm rel}}{\eta^2}. \tag{15}$$

If $t_{\rm cr} < t_{\rm newt}$, the FS will enter the adiabatic self-similar phase, described by Blandford & McKee (1976), right after $t_{\rm cr}$. We can then follow the radiation from the FS until the flow becomes non-relativistic.

2.2 Radiation

To obtain the observed radiation spectrum from the blast wave, we calculate the number of particles in each region, as a function of the lab-frame time. We then proceed to calculate the basic features of the synchrotron spectrum as a function of the thermodynamic quantities in each region.

2.2.1 Particle populations of regions 2 and 3

In order to calculate the radiation emanating from each region (2 and 3), we need to take account of the rate of influx of particles into regions 2 and 3 as a function of time.

For region 2 the number of particles as a function of time is easily found, as the FS is constantly moving at the speed of light and the density of the surrounding material is also constant. Therefore,

$$N_2(t_{\rm lab}) = \frac{4\pi}{3}\,c^3\,n_1\,t_{\rm lab}^3. \tag{16}$$

For region 3, we envision a layer of thickness δx of the unshocked ejecta, upstream from the RS (i.e. at lower radii), moving outwards with Lorentz factor η. The layer we are considering will have all been shocked within the lab-frame time δt. Therefore, the speed at which the RS is moving into the shell, as seen in the lab frame, will be $\delta x/\delta t$. We can write

$$\begin{aligned}\delta x &= \int_t^{t+\delta t} (v_{\rm ej} - v_2)\,{\rm d}t \approx \frac{c}{2}\int_t^{t+\delta t}\left(\frac{1}{\gamma_2^2} - \frac{1}{\eta^2}\right)\,{\rm d}t_{\rm lab}\\ &\approx \frac{c}{\eta^2\,t_{\rm rel}}\left[(t+\delta t)^2 - t^2\right]\\ &= \frac{c\,t^2}{\eta^2\,t_{\rm rel}}\left[\left(1 + \frac{\delta t}{t}\right)^2 - 1\right],\end{aligned} \tag{17}$$

where t is a lab-frame time for which $t_{\rm rel} < t < t_{\rm cr}$, $t_{\rm newt}$ and we have used again the approximation $\eta \gg \gamma_2$. For $\delta t \ll t$, we can then write

$$\frac{\delta x}{\delta t} \approx \frac{2\,c\,t}{\eta^2\,t_{\rm rel}} \equiv U^*. \tag{18}$$

In the lab frame, the rate of particles crossing the RS per unit time will be

$$\frac{{\rm d}N_3}{{\rm d}t_{\rm lab}} = 4\pi\,r^2\,U^*\,n_4 \tag{19}$$

and therefore $N_3(t_{\rm lab}) \propto t_{\rm lab}^2$.

However, by $t_{\rm rel}$ a fraction $t_{\rm rel}/(\eta^2\,\Delta t)$ of the ejecta have already been shocked.[1] An approximate formula that reconciles the scaling above with the percentage of particles already shocked by $t_{\rm rel}$ is

$$N_3(t_{\rm lab}) = N_{\rm T}\left[\left(1-\frac{t_{\rm rel}}{\eta^2\,\Delta t}\right)\frac{t_{\rm lab}^2-t_{\rm rel}^2}{t_{\rm cr}^2-t_{\rm rel}^2}+\frac{t_{\rm rel}}{\eta^2\,\Delta t}\right], \tag{20}$$

where $N_{\rm T}=E/\eta\,m_{\rm p}\,c^2$ is the total number of ejected particles. The above equation shows the correct asymptotic behaviour at $t_{\rm rel}$ and $t_{\rm cr}$ and obeys the scaling for N_3 at $t_{\rm lab}\gg t_{\rm rel}$.

2.2.2 *Synchrotron parameters*

The electrons (primary radiating particles) are assumed to be accelerated to a power-law energy distribution upon passage of the shocks (FS and RS). In the presence of a magnetic field, they will radiate via the synchrotron process. The total radiated power of a single electron of energy $\gamma_{\rm e}' m_{\rm e}c^2$ in the comoving frame is (see, for example, Rybicki & Lightman 1986)

$$P'_{\rm syn}\approx 2.66\times10^{-14}\,\gamma_{\rm e}'^2\,U'_{\rm B}, \tag{21}$$

where $U'_{\rm B}=4\,\epsilon_{\rm B}\,\gamma_2^2\,m_{\rm p}\,c^2\,n_1$ is the comoving magnetic energy density. The fraction of internal energy carried by the magnetic field is denoted by $\epsilon_{\rm B}$.

The minimum Lorentz factors of the electron distributions that populate regions 2 and 3 ($\gamma'_{\rm m-2}$ and $\gamma'_{\rm m-3}$, respectively) will be

$$\gamma'_{\rm m-2,3}=\gamma_{2,34}\,\frac{p-2}{p-1}\,\frac{m_{\rm p}}{m_{\rm e}}\,\epsilon_{\rm e}, \tag{22}$$

where p is the slope of the electron power-law distribution and $\epsilon_{\rm e}$ is the fraction of internal energy carried by the power-law electrons (e.g. Sari et al. 1998).

The electron Lorentz factor corresponding to the cooling frequency of the synchrotron spectrum can be estimated by considering those electrons which have radiated a considerable part of their energy, within the available comoving time:

$$\gamma'_{\rm c}\,m_{\rm e}\,c^2=P'_{\rm syn}(\gamma'_{\rm c})\,t'. \tag{23}$$

The comoving frequencies that these electron energies correspond to can be found using the formula for the synchrotron characteristic frequency:

$$\nu'_{\rm m,c}\approx 2.8\times10^6\,\gamma'^2_{\rm m,c}\,B', \tag{24}$$

where B' is the magnetic field that can be calculated through the equation

$$B'=\sqrt{8\pi\,U'_{\rm B}}. \tag{25}$$

The observed values of the characteristic frequencies are Doppler boosted and are obtained by multiplying the comoving values by the bulk Lorentz factor $\gamma_2(t_{\rm obs})$. Since regions 2 and 3 are in pressure equilibrium (same internal energy) and comoving, the observed value of the cooling frequency ($\nu_{\rm c}$) will be the same in both regions, provided that the value of $\epsilon_{\rm B}$ is common.

The peak flux of the synchrotron spectrum in the observer frame will be at either $\nu'_{\rm m}$ or $\nu'_{\rm c}$, whichever is smaller, and will have the value

$$F_{\rm m}=\gamma_2\,\frac{P'_{\rm syn}(\gamma'_{\rm m,c})}{\nu'_{\rm m,c}}\,\frac{N_{\rm beam}}{{\rm d}\Omega\,d^2}. \tag{26}$$

In the above equation, d is the distance to the source, $N_{\rm beam}=N\,{\rm d}\Omega/4\pi$ is the total number of particles whose radiation is beamed towards the observer and ${\rm d}\Omega=2\pi[1-\cos(\frac{\pi}{\gamma_2})]$ is the solid angle within which most of the radiation is being emitted.

In the case of a jetted outflow, the two effects of $N_{\rm beam}$ and ${\rm d}\Omega$ cancel out while $\gamma_2>1/\theta_{\rm j}$, where $\theta_{\rm j}$ is the half-opening angle of the jet. However, once $\gamma_2<1/\theta_{\rm j}$, ${\rm d}\Omega$ (the solid angle of the emission) keeps growing, while $N_{\rm beam}=N/2\,[1-\cos(\theta_{\rm j})]$, which stays constant. In other words, we account for the missing-flux effect after the edges of the jet become visible (Panaitescu et al. 1998), but not for sideways spreading (Rhoads 1999). The validity of this approach is reinforced by studies based on two-dimensional hydrodynamic simulations that find lateral spreading of the jet to be relatively unimportant, especially while the outflow is still relativistic (Granot et al. 2001; Zhang & MacFadyen 2009; Wygoda, Waxman & Frail 2011). We will only be concerned with top-hat jets, i.e. possible angular structure is ignored, and with on-axis observations. An off-axis observer will see the jet break at later times and will infer quite different properties for the outflow geometry, if the orientation with respect to the jet axis is not taken into account (e.g. van Eerten, Zhang & MacFadyen 2010).

Because GRBs are often of cosmological origin, redshift corrections on observer times, frequencies and fluxes need to be taken into account when calculating the observed spectra.

2.3 Power-law ejection

In this section, we show how the previous results can be generalized to address a source that has a power-law luminosity with time. We will confine our study to shells of ejecta with a uniform Lorentz factor, but variable density, so that at any given radius $\dot{M}\propto t_{\rm lab}^q$. The range of q is $-1<q<2$. For values of q below -1, the impulsive-explosion scenario is retrieved (Blandford & McKee 1976), while for $q\geq2$ the RS does not efficiently decelerate the ejecta. This range of q reflects all the possible values for which the model holds. However, not all values are equally plausible. The impulsive-ejection scenario is retrieved for $q\leq-1$ (Blandford & McKee 1976). Therefore, if the distribution of q is continuous, values close to, but greater than, -1 are expected. On the other hand, if $q>0$, the RS may still be accelerated to relativistic speeds, but the bulk of the ejected mass is essentially concentrated at the tail of the ejecta. A value close to 0 is predicted if the outflow is powered by a millisecond pulsar (Dai & Lu 1998), while fits to several *Swift* afterglows seem to indicate $q\sim-0.5$ (Zhang et al. 2006). This has been recently confirmed by Li et al. (2012). Furthermore, Curran et al. (2009) have found that half of the afterglows in their sample are consistent with energy injection, for which $-0.5<q<0$ was inferred. Therefore, we consider the range $-1<q<0$ to include a dominant fraction of the q distribution, in the case of prolonged ejection.

The total mass of the ejecta is $E/(\eta c^2)$ regardless of q, since the Lorentz factor of all the ejected material is the same. This leads to

$$\dot{M}=\frac{(q+1)\,E}{\eta\,c^2\,\Delta t^{q+1}}\,t_{\rm lab}^q. \tag{27}$$

[1] This can be verified in various ways. One is to consider the energy given to the CBM by the FS at $t_{\rm rel}$. It is found to be about a fraction $t_{\rm rel}/(\eta^2\,\Delta t)$ of the total blast-wave energy. This implies that a similar amount of energy has been subtracted from the unshocked ejecta, and since the total energy was initially homogeneously distributed in the ejected mass, the fraction of the width of the shell that has been shocked by $t_{\rm rel}$ is of the same order. Another, slightly more complicated way to derive this is by considering events in two reference frames moving with Lorentz factor η with respect to each other.

It follows that the lab-frame density of the ejected material is given by

$$n_4(t_{\rm lab}, t_{\rm ej}) = \frac{(q+1)\,E}{\eta\, c^2\, \Delta t^{q+1}}\, t_{\rm ej}^{q}\, \frac{(t_{\rm lab}-t_{\rm ej})^{-2}}{4\pi m_{\rm p} c^3}\,, \tag{28}$$

where $t_{\rm ej}$ marks the ejection time of any spherical layer of ejecta, and we have assigned $t_{\rm ej}=0$ to the leading layer. The next step is to calculate $t_{\rm rel,q}$, but to do that we first have to relate $t_{\rm lab}$ to $t_{\rm ej}$ for the layer that is being shocked by the RS. This can be done by realizing that the thickness of region 3 at any given lab-frame time is

$$c\, t_{\rm ej} = \int_0^{t_{\rm lab}} (v_{\rm ej} - v_2)\, {\rm d}t\,, \tag{29}$$

since the lab-frame Lorentz factor of the RS is γ_2. At $t_{\rm rel,q}$ the thickness will be

$$c \int_0^{t_{\rm rel,q}} \left(\frac{2}{\eta_2^2} - \frac{1}{2\eta^2}\right)\, {\rm d}t, \tag{30}$$

where we have approximated the lab-frame Lorentz factor of the RS with its value at $t_{\rm rel,q}$, i.e. $\eta/2$. From equations (29) and (30), we see that

$$t_{\rm rel,q} = \eta^2\, t_*\,, \tag{31}$$

where a factor 2/3 has been omitted in view of the normalization implied by equation (39) and t_* is the ejection time of the shell that is being shocked by the RS at the lab-frame time $t_{\rm rel,q}$.

Using equations (28) and (31), and by reasoning completely analogous to the case of steady ejection, we find

$$t_{\rm rel,q} = \left[\frac{(q+1)\,E}{\pi m_{\rm p} c^5\, n_1\, \Delta t^{q+1}}\, \eta^{-2(q+2)}\right]^{\frac{1}{2-q}}. \tag{32}$$

The scaling of the Lorentz factor of the shocked gas once the RS has become relativistic is $\gamma_2^2 \propto t_{\rm lab}^{\frac{q-2}{q+2}}$ (Blandford & McKee 1976) leading to

$$\gamma_2(t_{\rm lab}) = \frac{\eta}{2}\left(\frac{t_{\rm rel,q}}{t_{\rm lab}}\right)^{\frac{2-q}{2(2+q)}}. \tag{33}$$

Another useful consistency check at this point can be performed by combining equations (32) and (33). Then one retrieves the exact same scaling for γ_2 as in equation 58 of Blandford & McKee (1976).

Knowing the scaling of γ_2 [and therefore also that of γ_{34} through equation (5)], we can reconstruct the profile of the density that the RS is moving inside the ejected shell. We find

$$n'_{4-{\rm RS}} = n_1\, \frac{\eta^2}{4}\left(\frac{t_{\rm rel,q}}{t_{\rm lab}}\right)^{\frac{2(2-q)}{2+q}}. \tag{34}$$

The speed at which the RS is moving into the shell can be estimated in a manner similar to that in the case of steady ejection,

$$\begin{aligned}
\delta x &= \frac{c}{2}\int_t^{t+\delta t} \frac{1}{\gamma_2^2}\, {\rm d}t \\
&= \frac{2\,c}{\eta^2}\, t_{\rm rel,q}^{\frac{q-2}{q+2}}\, \frac{2+q}{4}\, \left[(t+\delta t)^{\frac{4}{2+q}} - t^{\frac{4}{2+q}}\right] \\
&= \frac{2\,c}{\eta^2}\, t_{\rm rel,q}^{\frac{q-2}{q+2}}\, \frac{2+q}{4}\, t^{\frac{4}{2+q}} \left[\left(1+\frac{\delta t}{t}\right)^{\frac{4}{2+q}} - 1\right] \Rightarrow \\
U^* &= \frac{2c}{\eta^2}\left(\frac{t_{\rm rel,q}}{t_{\rm lab}}\right)^{\frac{q-2}{q+2}}.
\end{aligned} \tag{35}$$

The crossing time of the shell can be calculated in a similar way to the $q=0$ case,

$$t_{\rm cr,q} = \left(\frac{2}{q+2}\, t_{\rm rel,q}^{\frac{2-q}{2+q}}\, \Delta t\, \eta^2\right)^{\frac{q+2}{4}}. \tag{36}$$

We can now derive the scaling for the number of particles in region 3 as a function of time,

$$\frac{{\rm d}N_3}{{\rm d}t} = 4\pi c^2 t^2\, U^*\, n_{4-{\rm RS}} \;\Rightarrow\; N_3 \propto t_{\rm lab}^{\frac{4(q+1)}{q+2}}. \tag{37}$$

As in the case of steady ejection, we construct a formula that obeys this scaling once the RS is relativistic while it takes into account the particles already shocked before $t_{\rm rel,q}$ and satisfies the conservation of particle number at $t_{\rm cr,q}$

$$N_3(t_{\rm lab}) = N_{\rm T}\left[\left(1-\frac{N_{\rm rel}}{N_{\rm T}}\right)\frac{t_{\rm lab}^{y} - t_{\rm rel,q}^{y}}{t_{\rm cr,q}^{y} - t_{\rm rel,q}^{y}} + \frac{N_{\rm rel}}{N_{\rm T}}\right], \tag{38}$$

where $N_{\rm rel} = N_3(t_{\rm rel,q})$ is the number of ejected particles that have been shocked by $t_{\rm rel,q}$ and $y = \frac{4(q+1)}{q+2}$. To get an estimate of $N_3(t_{\rm rel,q})$, we use equations (27) and (31)

$$\begin{aligned}
N_3(t_{\rm rel,q}) &= \frac{1}{m_{\rm p}}\int_0^{t_*} \dot{M}\,{\rm d}t = N_{\rm T}\,\Delta t^{-(q+1)}\, t_*^{q+1} \\
&= N_{\rm T}\left(\frac{t_{\rm rel,q}}{\eta^2\,\Delta t}\right)^{q+1}.
\end{aligned} \tag{39}$$

Comparing this result with the steady-ejection scenario, we are able to specify the normalization factor of equation (31).

One can verify that all the expressions for the power-law ejection can be reduced to the ones corresponding to steady ejection when $q=0$.

3 LIGHT CURVES FROM THE FS AND RS

In this section, we present results from the numerical implementation of the equations presented in the previous section. We explore the extent to which emission from the FS and the RS can explain the diversity of observations during the plateau phase. We find that RS light curves are generally different than those of the FS. Therefore, when the RS contribution is significant, a wider range of possibilities exist for the observed decay indices and breaks. We also find that the dynamics of the intermediate phase allows for very different decay indices in optical and X-ray frequencies (discussed in Panaitescu & Vestrand 2011), as long as a critical frequency of the spectrum lies between these bands. This result holds both for the FS and the RS. We show that the interplay between FS and RS can lead to injection breaks accompanied by spectral evolution. Some of these features have been interpreted as evidence for the presence of additional radiation mechanisms. Here we show how they arise naturally, even in the simplest form of the thick-shell scenario.

Construction of spectra as a function of time follows from calculating $F_{\rm m}$, $\nu_{\rm m}$ and $\nu_{\rm c}$ (Sari et al. 1998). Self-absorption of synchrotron photons is ignored, as we are mostly interested in the optical and X-ray behaviour observed in the 'plateau' phase, during the early afterglow. The influence of self-absorption on optical frequencies can be excluded by the fact that after the injection break, the slopes of the observed light curves are typically negative. Spectral breaks are assumed to have infinite sharpness, for simplicity.

In the case of jetted outflows, the blast-wave energy E stands for the isotropic equivalent of the 'real' energy content of the blast wave which is $E_{\rm bw} = E\Omega_{\rm j}/4\pi$, with $\Omega_{\rm j}$ denoting the solid angle of the pair of jets.

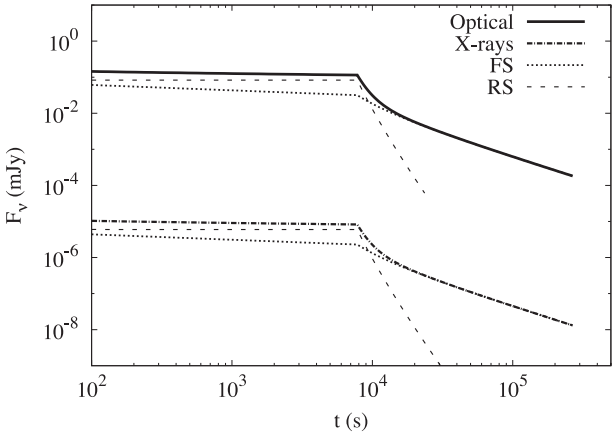

Figure 1. Optical (top) and X-ray (bottom) light curves before and after the injection break (at approximately 8×10^3 s). The optical frequency is 5×10^{14} Hz, while the X-ray frequency is 2×10^{18} Hz. The contributions of the FS (dotted line) and RS (dashed line) are depicted for both. Physical parameters are $E = 10^{51}$ erg, $n_1 = 50\,\mathrm{cm}^{-3}$, $\Delta t = 5 \times 10^3$ s, $\eta = 600$, $q = 0$, $\epsilon_\mathrm{e} = \epsilon_\mathrm{B} = 0.1$, $p = 2.3$, $\theta_\mathrm{j} = 90°$, $d = 10^{28}$ cm and $z = 0.56$.

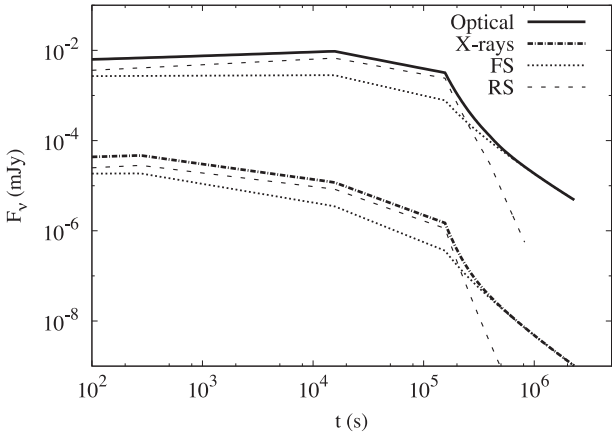

Figure 2. Similar to Fig. 1 but for different physical parameters. Two achromatic breaks are present, the jet break around 10^4 s and the injection break around 10^5 s. There is also a break in the X-ray light curve (around 3×10^2 s), due to the crossing of ν_c, with no corresponding optical feature. Physical parameters are $E = 10^{52}$ erg, $n_1 = 0.04\,\mathrm{cm}^{-3}$, $\Delta t = 10^5$ s, $\eta = 1000$, $q = -0.3$, $\epsilon_\mathrm{e} = 0.2$, $\epsilon_\mathrm{B} = 0.007$, $p = 2.2$, $\theta_\mathrm{j} = 7°$, $d = 10^{28}$ cm and $z = 0.56$.

3.1 Simple light curves with the same temporal index

A simultaneous steepening in the light curves of optical and X-ray data can be interpreted either as a jet break or an 'injection' break (Zhang et al. 2006; Racusin et al. 2009). There are cases where the decay indices before and after the break clearly favour the second interpretation. In Fig. 1, we present light curves at optical and X-ray frequencies before and after an injection break, calculated using the formulas in the previous section. The light curves are similar in these two bands because optical and X-ray frequencies lie above ν_m and ν_c, both in the FS and the RS. Therefore, spectral indices before and after the break remain constant. A notable feature of the RS emission is the rapid decay after the injection break, as expected, due to adiabatic and radiative cooling. The decay index can become as steep as about -5. The physical parameters for this example (see the caption of Fig. 1) have been chosen such that the resulting light curves are not complicated by effects like the crossing of critical frequencies or jet breaks.

The case presented in Fig. 1 is one of the simplest possible. However, despite the simplicity, both the FS and the RS contribute significantly to the observed flux at optical and X-ray frequencies. In fact, radiation from region 3 (ejecta shocked by the RS) is prominent before the injection break, soon after which the radiation from the FS becomes dominant. Therefore, this example demonstrates how light curves in optical and X-rays with the same temporal index can be influenced by radiation from both the FS and the RS, but still appear featureless (apart from the injection break). This has been previously interpreted as an indication of one region (typically region 2) dominating the spectrum (Panaitescu & Vestrand 2011), something which is not necessarily the case.

3.2 Light curves with different temporal indices, chromatic and achromatic breaks

In Fig. 2, we present light curves for a set of physical parameters that results in different behaviour in the optical than in the X-rays. Namely, the X-ray light curve has one extra break, compared to the optical, due to the passage of ν_c through the X-ray band both in regions 2 and 3. After that chromatic break, there are two achromatic ones, first due to the edges of the jet becoming visible (jet break at 10^4 s) and then due to the RS crossing the ejecta (injection break at 1.5×10^5 s).

Fig. 2 demonstrates clearly how chromatic breaks and different decay indices between optical and X-ray light curves are possible. The break in the X-ray light curve at about 3×10^2 s is caused by the crossing of ν_c. However, such a break is accompanied by a change in the spectral index of the X-ray band, something not always seen during chromatic X-ray breaks (Nousek et al. 2006), pointing to a different origin for the break in those cases. Fig. 2 shows also an example of light curves in optical and X-ray frequencies having distinct decay indices, their difference in this case bigger than 0.4. For comparison, in the canonical (adiabatic) afterglow phase, the difference is 0.25, for $\nu_\mathrm{m} < \nu_\mathrm{o} < \nu_\mathrm{c} < \nu_\mathrm{x}$ (Granot & Sari 2002). This has been previously reported for FS emission (e.g. Zhang et al. 2006; Panaitescu & Vestrand 2012). Here, we show how the same feature can also be produced if the RS dominates emission in both bands.

3.3 Achromatic breaks with spectral evolution

In Fig. 3, we present light curves for another set of parameters. The temporal indices in optical and X-ray bands are the same from 10^3 s onwards. Before that, there are two chromatic breaks in the optical light curve due to the passage of ν_c (both in regions 2 and 3) and the passage of ν_m (only in region 2). Immediately after the injection break at 1.5×10^4 s, emission from the RS fades and the spectrum is dominated by emission from the FS. However, whereas in the X-rays the spectral index does not change (assuming that p is the same in both regions), it does in the optical. This happens because the optical frequency (5×10^{14} Hz) lies in different power laws of the spectrum in the FS and the RS, while the X-ray frequency (2×10^{18} Hz) does not. Therefore, frequency-dependent behaviour of the spectral index is possible during the injection break, regardless of the decay indices in optical and X-ray light curves.

3.4 The influence of a different ϵ_B

Magnetic fields in the blast wave are understood to be the result of amplification of a pre-existing seed field in the unshocked gas. The

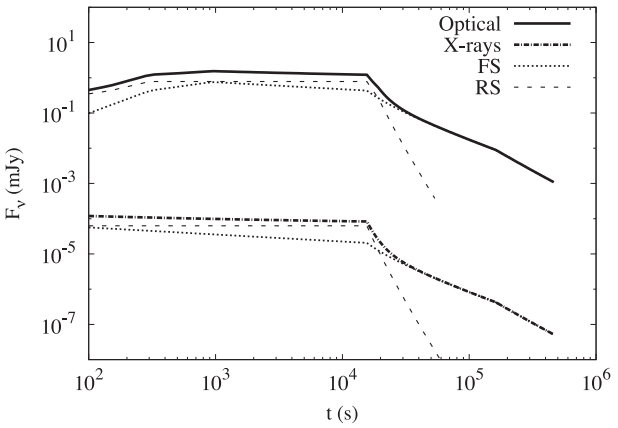

Figure 3. Similar to Fig. 1 but for different physical parameters. The injection break can be seen at 1.5×10^4 s, while the jet break occurs at 1.5×10^5 s. Physical parameters are $E = 10^{52}$ erg, $n_1 = 6\,\mathrm{cm}^{-3}$, $\Delta t = 10^4$ s, $\eta = 1000, q = 0, \epsilon_e = 0.2, \epsilon_B = 0.05, p = 2.4, \theta_j = 30^\circ, d = 10^{28}$ cm and $z = 0.56$.

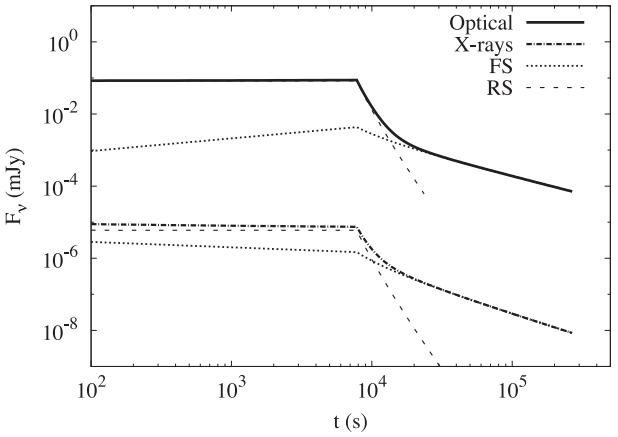

Figure 4. Similar to Fig. 1, only here $\epsilon_{B2} = 3 \times 10^{-4}$, while in region 3 ϵ_B has retained the value of 0.1.

CBM is expected to carry a significantly lower degree of magnetization than the ejecta, especially in the case of magnetic acceleration of the outflow (Komissarov et al. 2009). Under these conditions, having $\epsilon_{B2} \ll \epsilon_{B3}$ becomes a very realistic possibility. In this section, we explore the influence of a different ϵ_B in the two radiating regions. In Fig. 4, we present light curves for a physical scenario identical with that of Section 3.1 apart from the value of ϵ_B, which for region 2 is now about 300 times smaller. However, whereas in the optical this results in the FS flux being much smaller than that of the RS, this is not the case in the X-rays, where emission from region 2 is almost as strong as it was when $\epsilon_{B2} = 0.1$. After the injection break, the behaviour of the light curves in the optical and X-rays is different. In the X-rays the transition to the adiabatic phase is relatively smooth, but in the optical there is a steep segment of the light curve as the total flux of the blast wave drops by about two orders of magnitude to recover the levels of the FS. The reason for this can be found in the dependences of the spectral parameters on ϵ_B. These are presented in Table 1. The range of the $\epsilon_{B2}/\epsilon_{B3}$ ratio for which such a disparity between optical and X-ray light curves becomes noticeable is limited and also depends on other model parameters. Roughly, it covers two orders of magnitude, from about 0.1 to 0.001. It follows that it is quite difficult to suppress radiation from any region in high frequencies, through a low value for ϵ_B. Instead, both the FS and the RS are expected to contribute significantly for $10^{-3} < \epsilon_{B2}/\epsilon_{B3} < 10^3$. On the other hand, flux in the optical is much more sensitive to the value of ϵ_B.

3.5 General remarks

In all models presented in this section, the FS and the RS share the same microphysics parameters ϵ_e and p. The light curves can become more complicated when this constraint is removed. Different values of ϵ_e would effectively suppress radiation from the region with the lower efficiency. Different values of p can influence the decay indices, but also the flux levels, and may lead to the inference of spectral evolution during the injection break.

In all the light curves presented in this section, a common feature is the considerable contribution from the RS, which by the end of the plateau phase dominates the emission. An inevitable consequence in such cases is the characteristic drop of the combined light curve immediately after the injection break, due to the rapid decline of the RS emission. The sharpness of the drop in the combined light curve is dictated by the relative level of the FS emission, which soon after the injection break dominates the emission. We consider this characteristic drop, right after the injection break, to be a strong indication of the RS contributing significantly to the flux detected at the end of the plateau phase. Examples of optical afterglow light curves that clearly exhibit such a behaviour can be seen in GRB 080928 and GRB 090423 (e.g. Panaitescu & Vestrand 2011) which are explored further in Section 5.

4 FORMULAS FOR THE OBSERVED SPECTRA

Calculations of the RS emission have been presented in the past and sometimes have been used to fit model parameters to data (Meszaros & Rees 1997; Panaitescu et al. 1998; Sari & Piran 1999; Chevalier & Li 2000; Kobayashi & Sari 2000; Kumar & Panaitescu 2003; Zhang et al. 2006; Uhm 2011). However, an element that seems to be missing from the literature is flux scalings for the FS and the RS in the intermediate dynamical phase, when the RS is relativistic. In this section we present normalized scalings for the three spectral parameters (F_m, ν_m and ν_c) introduced in Section 2, of both the FS and the RS. We also present flux formulas for all optically thin power-law segments (PLS) in the slow ($\nu_m < \nu_c$) and fast ($\nu_c < \nu_m$) cooling case.

Table 1 contains the analytic expressions for the dependences of F_m, ν_m and ν_c on the physical parameters of the model. The values of the spectral parameters are calculated in the observer frame. Under the assumption of pressure equilibrium between regions 2 and 3, the cooling frequency is the same in both regions, provided that they share the same ϵ_B. The formulas presented in Table 1 can be used to calculate the flux at every possible PLS of the synchrotron spectra that originate from the FS and the RS. The results are presented in Table 2. Note that in most segments, the light curves are expected to be flat to inverted, for moderate values of q (close to 0). When $\nu < \nu_m$, ν_c in the FS, the light curves rise more steeply. The fact that ν_m of region 3 is constant with time, regardless of the value of q (see Table 1), implies that the temporal profiles of two consecutive PLS (those connected at ν_m) are identical, both in the slow cooling and the fast cooling case. It is easy to check that the temporal indices for the spectral parameters (Table 1) and the flux in individual PLS of the spectrum (Table 2) converge to the impulsive-ejection scenario (thin shell) when $q = -1$ (see, for example, Granot & Sari 2002).

Table 1. Analytic formulas for $F_{\rm m}$, $\nu_{\rm m}$ and $\nu_{\rm c}$ in the observer frame, during energy injection, both for the FS and the RS. Results are presented for all the physical parameters of the model.

FS (region 2)

$$F_{\rm m} = 2.593\times10^{-1}\left(\frac{2}{q+2}\right)^{q+1}(q+1)\,\epsilon_{\rm B}^{\frac{1}{2}}\,E_{50}\,n_1^{\frac{1}{2}}\,\Delta t^{-(q+1)}\,t_{\rm obs}^{q+1}\,(1+z)^{-q}\,d_{28}^{-2}\ {\rm mJy}$$

$$\nu_{\rm m} = 6.429\times10^{21}\left(\frac{2}{q+2}\right)^{\frac{q-2}{2}}(q+1)^{\frac{1}{2}}\left(\frac{p-2}{p-1}\right)^{2}\epsilon_{\rm e}^{2}\,\epsilon_{\rm B}^{\frac{1}{2}}\,E_{50}^{\frac{1}{2}}\,\Delta t^{-\frac{(q+1)}{2}}\,t_{\rm obs}^{\frac{q-2}{2}}\,(1+z)^{-q/2}\ {\rm Hz}$$

$$\nu_{\rm c} = 1.018\times10^{15}\left(\frac{2}{q+2}\right)^{-\frac{(q+2)}{2}}(q+1)^{-\frac{1}{2}}\,\epsilon_{\rm B}^{-\frac{3}{2}}\,E_{50}^{-\frac{1}{2}}\,n_1^{-1}\,\Delta t^{\frac{q+1}{2}}\,t_{\rm obs}^{-\frac{(q+2)}{2}}\,(1+z)^{q/2}\ {\rm Hz}$$

RS (region 3)

$$F_{\rm m} = 3.255\times10^{4}\left(\frac{2}{q+2}\right)^{\frac{q-2}{4}}(q+1)^{\frac{1}{4}}\,\epsilon_{\rm B}^{\frac{1}{2}}\,E_{50}^{\frac{5}{4}}\,n_1^{\frac{1}{4}}\,\eta^{-1}\,\Delta t^{-\frac{5(q+1)}{4}}\,t_{\rm obs}^{\frac{5q+2}{4}}\,(1+z)^{\frac{2-5q}{4}}\,d_{28}^{-2}\ {\rm mJy}$$

$$\nu_{\rm m} = 9.173\times10^{11}\left(\frac{p-2}{p-1}\right)^{2}\epsilon_{\rm e}^{2}\,\epsilon_{\rm B}^{\frac{1}{2}}\,n_1^{\frac{1}{2}}\,\eta^{2}\,(1+z)^{-1}\ {\rm Hz}$$

$$\nu_{\rm c} = 1.018\times10^{15}\left(\frac{2}{q+2}\right)^{-\frac{(q+2)}{2}}(q+1)^{-\frac{1}{2}}\,\epsilon_{\rm B}^{-\frac{3}{2}}\,E_{50}^{-\frac{1}{2}}\,n_1^{-1}\,\Delta t^{\frac{q+1}{2}}\,t_{\rm obs}^{-\frac{(q+2)}{2}}\,(1+z)^{q/2}\ {\rm Hz}$$

Table 2. Flux (in mJy) at every PLS of the FS and the RS in the observer frame, during energy injection. The factors C_F, $C_{\rm m}$ and $C_{\rm c}$ are the numerical constants from Table 1, appearing in the formulas of $F_{\rm m}$, $\nu_{\rm m}$ and $\nu_{\rm c}$, respectively. The extra subscripts (FS and RS) denote the region of emission which corresponds to the upper (FS) and lower (RS) half of Table 1.

FS (region 2)

Slow cooling

$\nu<\nu_{\rm m}<\nu_{\rm c}$ $\quad F_\nu = C_{F,{\rm FS}}\,C_{\rm m,FS}^{-1/3}\left(\frac{2}{q+2}\right)^{\frac{5q+8}{6}}(q+1)^{\frac{5}{6}}\left(\frac{p-2}{p-1}\right)^{-\frac{2}{3}}\epsilon_{\rm e}^{-\frac{2}{3}}\,\epsilon_{\rm B}^{\frac{1}{3}}\,E_{50}^{\frac{5}{6}}\,n_1^{\frac{1}{2}}\,\Delta t^{-\frac{5(q+1)}{6}}\,t_{\rm obs}^{\frac{5q+8}{6}}\,\nu^{\frac{1}{3}}\,(1+z)^{-\frac{5q}{6}}\,d_{28}^{-2}$

$\nu_{\rm m}<\nu<\nu_{\rm c}$ $\quad F_\nu = C_{F,{\rm FS}}\,C_{\rm m,FS}^{(p-1)/2}\left(\frac{2}{q+2}\right)^{\frac{p(q-2)+3(q+2)}{4}}(q+1)^{\frac{p+3}{4}}\left(\frac{p-2}{p-1}\right)^{p-1}\epsilon_{\rm e}^{p-1}\,\epsilon_{\rm B}^{\frac{p+1}{4}}\,E_{50}^{\frac{p+3}{4}}\,n_1^{\frac{1}{2}}\,\Delta t^{-\frac{(p+3)(q+1)}{4}}\,t_{\rm obs}^{\frac{p(q-2)+3(q+2)}{4}}\,\nu^{\frac{1-p}{2}}\,(1+z)^{-\frac{q(p+3)}{4}}\,d_{28}^{-2}$

$\nu_{\rm m}<\nu_{\rm c}<\nu$ $\quad F_\nu = C_{F,{\rm FS}}\,C_{\rm c,FS}^{1/2}\,C_{\rm m,FS}^{(p-1)/2}\left(\frac{2}{q+2}\right)^{\frac{qp+2(2+q-p)}{4}}(q+1)^{\frac{p+2}{4}}\left(\frac{p-2}{p-1}\right)^{p-1}\epsilon_{\rm e}^{p-1}\,\epsilon_{\rm B}^{\frac{p-2}{4}}\,E_{50}^{\frac{p+2}{4}}\,\Delta t^{-\frac{(p+2)(q+1)}{4}}\,t_{\rm obs}^{\frac{qp+2(2+q-p)}{4}}\,\nu^{-\frac{p}{2}}\,(1+z)^{-\frac{q(p+2)}{4}}\,d_{28}^{-2}$

Fast cooling

$\nu<\nu_{\rm c}<\nu_{\rm m}$ $\quad F_\nu = C_{F,{\rm FS}}\,C_{\rm c,FS}^{-1/3}\left(\frac{2}{q+2}\right)^{\frac{7q+8}{6}}(q+1)^{\frac{7}{6}}\,\epsilon_{\rm B}\,E_{50}^{\frac{7}{6}}\,n_1^{\frac{5}{6}}\,\Delta t^{-\frac{7(q+1)}{6}}\,t_{\rm obs}^{\frac{7q+8}{6}}\,\nu^{\frac{1}{3}}\,(1+z)^{-\frac{7q}{6}}\,d_{28}^{-2}$

$\nu_{\rm c}<\nu<\nu_{\rm m}$ $\quad F_\nu = C_{F,{\rm FS}}\,C_{\rm c,FS}^{1/2}\left(\frac{2}{q+2}\right)^{\frac{3q+2}{4}}(q+1)^{\frac{3}{4}}\,\epsilon_{\rm B}^{-\frac{1}{4}}\,E_{50}^{\frac{3}{4}}\,\Delta t^{-\frac{3(q+1)}{4}}\,t_{\rm obs}^{\frac{3q+2}{4}}\,\nu^{-\frac{1}{2}}\,(1+z)^{-\frac{3q}{4}}\,d_{28}^{-2}$

$\nu_{\rm c}<\nu_{\rm m}<\nu$ $\quad F_\nu = C_{F,{\rm FS}}\,C_{\rm c,FS}^{1/2}\,C_{\rm m,FS}^{(p-1)/2}\left(\frac{2}{q+2}\right)^{\frac{qp+2(2+q-p)}{4}}(q+1)^{\frac{p+2}{4}}\left(\frac{p-2}{p-1}\right)^{p-1}\epsilon_{\rm e}^{p-1}\,\epsilon_{\rm B}^{\frac{p-2}{4}}\,E_{50}^{\frac{p+2}{4}}\,\Delta t^{-\frac{(p+2)(q+1)}{4}}\,t_{\rm obs}^{\frac{qp+2(2+q-p)}{4}}\,\nu^{-\frac{p}{2}}\,(1+z)^{-\frac{q(p+2)}{4}}\,d_{28}^{-2}$

RS (region 3)

Slow cooling

$\nu<\nu_{\rm m}<\nu_{\rm c}$ $\quad F_\nu = C_{F,{\rm RS}}\,C_{\rm m,RS}^{-1/3}\left(\frac{2}{q+2}\right)^{\frac{q-2}{4}}(q+1)^{\frac{1}{4}}\left(\frac{p-2}{p-1}\right)^{-\frac{2}{3}}\epsilon_{\rm e}^{-\frac{2}{3}}\,\epsilon_{\rm B}^{\frac{1}{3}}\,E_{50}^{\frac{5}{4}}\,n_1^{\frac{1}{12}}\,\eta^{-\frac{5}{3}}\,\Delta t^{-\frac{5(q+1)}{4}}\,t_{\rm obs}^{\frac{5q+2}{4}}\,\nu^{\frac{1}{3}}\,(1+z)^{\frac{10-15q}{12}}\,d_{28}^{-2}$

$\nu_{\rm m}<\nu<\nu_{\rm c}$ $\quad F_\nu = C_{F,{\rm RS}}\,C_{\rm m,RS}^{(p-1)/2}\left(\frac{2}{q+2}\right)^{\frac{q-2}{4}}(q+1)^{\frac{1}{4}}\left(\frac{p-2}{p-1}\right)^{p-1}\epsilon_{\rm e}^{p-1}\,\epsilon_{\rm B}^{\frac{p+1}{4}}\,E_{50}^{\frac{5}{4}}\,n_1^{\frac{p}{4}}\,\eta^{p-2}\,\Delta t^{-\frac{5(q+1)}{4}}\,t_{\rm obs}^{\frac{5q+2}{4}}\,\nu^{\frac{1-p}{2}}\,(1+z)^{\frac{4-2p-5q}{4}}\,d_{28}^{-2}$

$\nu_{\rm m}<\nu_{\rm c}<\nu$ $\quad F_\nu = C_{F,{\rm RS}}\,C_{\rm c,RS}^{1/2}\,C_{\rm m,RS}^{(p-1)/2}\left(\frac{2}{q+2}\right)^{-1}\left(\frac{p-2}{p-1}\right)^{p-1}\epsilon_{\rm e}^{p-1}\,\epsilon_{\rm B}^{\frac{p-2}{4}}\,E_{50}\,n_1^{\frac{p-2}{4}}\,\eta^{p-2}\,\Delta t^{-(q+1)}\,t_{\rm obs}^{q}\,\nu^{-\frac{p}{2}}\,(1+z)^{\frac{2-2q-p}{2}}\,d_{28}^{-2}$

Fast cooling

$\nu<\nu_{\rm c}<\nu_{\rm m}$ $\quad F_\nu = C_{F,{\rm RS}}\,C_{\rm c,RS}^{-1/3}\left(\frac{2}{q+2}\right)^{\frac{5q-2}{12}}(q+1)^{\frac{5}{12}}\,\epsilon_{\rm B}\,E_{50}^{\frac{17}{12}}\,n_1^{\frac{7}{12}}\,\eta^{-1}\,\Delta t^{-\frac{17(q+1)}{12}}\,t_{\rm obs}^{\frac{17q+10}{12}}\,\nu^{\frac{1}{3}}\,(1+z)^{\frac{6-17q}{12}}\,d_{28}^{-2}$

$\nu_{\rm c}<\nu<\nu_{\rm m}$ $\quad F_\nu = C_{F,{\rm RS}}\,C_{\rm c,RS}^{1/2}\left(\frac{2}{q+2}\right)^{-1}\epsilon_{\rm B}^{-\frac{1}{4}}\,E_{50}\,n_1^{-\frac{1}{4}}\,\eta^{-1}\,\Delta t^{-(q+1)}\,t_{\rm obs}^{q}\,\nu^{-\frac{1}{2}}\,(1+z)^{\frac{1-2q}{2}}\,d_{28}^{-2}$

$\nu_{\rm c}<\nu_{\rm m}<\nu$ $\quad F_\nu = C_{F,{\rm RS}}\,C_{\rm c,RS}^{1/2}\,C_{\rm m,RS}^{(p-1)/2}\left(\frac{2}{q+2}\right)^{-1}\left(\frac{p-2}{p-1}\right)^{p-1}\epsilon_{\rm e}^{p-1}\,\epsilon_{\rm B}^{\frac{p-2}{4}}\,E_{50}\,n_1^{\frac{p-2}{4}}\,\eta^{p-2}\,\Delta t^{-(q+1)}\,t_{\rm obs}^{q}\,\nu^{-\frac{p}{2}}\,(1+z)^{\frac{2-2q-p}{2}}\,d_{28}^{-2}$

4.1 The $F_{\rm b}$–$t_{\rm b}$ relation

Accumulating observations of plateau afterglows have allowed for a more systematic study of the behaviour revealed by *Swift* (e.g. Dainotti, Cardone & Capozziello 2008). Panaitescu & Vestrand (2011) have found that plateau afterglows, 17 in their sample, obey the relation $F_{\rm b}\propto t_{\rm b}^{-1\pm0.5}$, where $F_{\rm b}$ is the optical flux at the injection break and $t_{\rm b}$ is the observed time of the break.[2] More recently, Li et al. (2012) studied the $F_{\rm b}$–$t_{\rm b}$ relation for a sample of 39 afterglows with a shallow decay in the optical. They derive a much tighter relation, $F_{\rm b}\propto t_{\rm b}^{-0.78\pm0.08}$. This relation falls within the range of Panaitescu & Vestrand (2011) but carries a much smaller uncertainty, by almost an order of magnitude. In this section, we derive model predictions for the $F_{\rm b}$–$t_{\rm b}$ relation and compare them to the aforementioned studies.

Given that the observed time of the injection break (equation 15) is dominated by the time-scale of the ejection and ignoring redshift

[2] The uncertainty is mainly caused by the determination of the break time, rather than the errors of photometric data. In Fig. 2, we show an example of how narrow jet angles and long ejection times can result in consecutive achromatic breaks that can be ambiguously interpreted.

Table 3. Dependence of the observed monochromatic flux at the end of the plateau phase on the duration of ejection ($F_b \propto \Delta t^x$). Values of x are presented for every PLS from the FS and the RS, both in the case of *slow* and *fast* cooling.

	FS	RS
Slow cooling		
$\nu < \nu_m < \nu_c$	$\frac{1}{2}$	$-\frac{3}{4}$
$\nu_m < \nu < \nu_c$	$-\frac{3(p-1)}{4}$	$-\frac{3}{4}$
$\nu_m < \nu_c < \nu$	$\frac{2-3p}{4}$	-1
Fast cooling		
$\nu < \nu_c < \nu_m$	$\frac{1}{6}$	$-\frac{7}{12}$
$\nu_c < \nu < \nu_m$	$-\frac{1}{4}$	-1
$\nu_c < \nu_m < \nu$	$\frac{2-3p}{4}$	-1

effects, we can approximate $t_b \approx \Delta t$. Using the information of Table 2, we analytically derive the scalings of $F_b = F(\Delta t)$ for the FS and the RS, both in the case of slow and fast cooling and present them in Table 3. A readily apparent feature of these scalings is the absence of q from the exponents of Δt. A quick inspection of Table 1 reveals that in fact all spectral parameters of both regions are independent of q at the injection break, except for the normalization factors which are of order unity. The reason for this is that at the end of the plateau phase (approximated by Δt), the parameters γ_2, t_{cr}, $n_4(t_{lab}, t_{ej})$ and of course n_1 are either independent or very weakly dependent on q (see equations 28, 32, 33, 36). Therefore, the jump conditions close to the injection break, at both shocks, give rise to (thermo)dynamics of the blast wave (regions 2 and 3) that are independent of the details of energy injection. Consequently, spectra from the FS and the RS at the injection break carry no information on how the power was provided by the central engine. This makes the $F_b - t_b$ relation an even more powerful diagnostic of the physics of the plateau phase since it is insensitive to the exact history of energy injection, which may vary from source to source.

The relation between the scalings presented in Table 3 and the findings of Panaitescu & Vestrand (2011) and Li et al. (2012) can be better understood through Fig. 5. In that figure, we show how the index of the $F_b - t_b$ relation depends on the value of p for all the PLS of the FS and the RS, both for slow and fast cooling. We also present the observationally inferred values of the index, for both studies. In Fig. 5, we see that model predictions, for some of the PLS of the FS, lie outside the shaded regions. The curves that, at least partially, lie within the shaded regions correspond to spectrum configurations where the synchrotron characteristic frequency ν_m is smaller than optical frequencies, at the end of the plateau. As long as that condition is fulfilled (which is very likely to be the case, especially for long-lived plateaus), the FS can account for the $F_b - t_b$ relation of Panaitescu & Vestrand (2011). However, FS emission can only reproduce the scaling of Li et al. (2012) if $\nu_m < \nu_o < \nu_c$ and $p < 2.2$. In all other cases, the predictions for the FS are at odds with the relation of Li et al. (2012).

On the other hand, the RS shows less diversity in the possible values of the index. In fact, the relation of Panaitescu & Vestrand (2011) is not just possible, but inevitable, regardless of the value of p and the relevant PLS. However, the scaling of Li et al. (2012) is achieved only if $\nu_m < \nu_o < \nu_c$, but for any value of p. If $\nu_c < \nu_o$, the predicted relation is slightly steeper with an index of -1, regardless of the value of ν_m. The findings of both groups (and especially these of Li et al. 2012) can be better explained if the ejecta shocked by the RS are dominating the emission during the plateau phase.

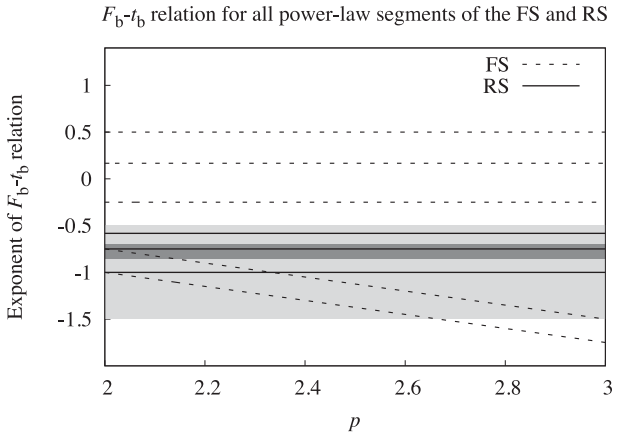

Figure 5. Index of the $F_b - t_b$ relation as a function of p, for all PLS of the FS and the RS. The lightly shaded region contains the range of values allowed by the scaling of Panaitescu & Vestrand (2011), while the darker region denotes the scaling of Li et al. (2012). The five dashed lines correspond to the five possible indices for the FS, as presented in Table 3. From top to bottom: (i) $\nu < \nu_m < \nu_c$, (ii) $\nu < \nu_c < \nu_m$, (iii) $\nu_c < \nu < \nu_m$, (iv) $\nu_m < \nu < \nu_c$, (v) $\nu_m,\ \nu_c < \nu$. The three solid lines depict the three possible (independent of p) indices for the RS and correspond to (again, from top to bottom) (i) $\nu < \nu_c < \nu_m$, (ii) $\nu < \nu_m < \nu_c$ and $\nu_m < \nu < \nu_c$, (iii) $\nu_c < \nu < \nu_m$ and $\nu_m,\ \nu_c < \nu$.

Recently, Dainotti et al. (2013) have updated their study of the $F_b - t_b$ relation as measured by the X-ray Telescope (XRT) aboard *Swift*, in X-ray frequencies. Using a sample of 101 afterglows, the 1σ range of the index is found to be $-1.07^{+0.09}_{-0.14}$. According to Table 3 and Fig. 5, the prediction for the RS falls within this range as long as the XRT bandpass (0.3−10 keV) lies above ν_m and ν_c (something likely for a wide range of parameters), for any value of p. The same spectral configuration ($\nu_m,\ \nu_c < \nu_x$) is also favoured in the case of the FS. Interestingly, the necessary condition for the FS prediction to be reconciled with this finding is the same as in the Li et al. (2012) relation for optical breaks, $p < 2.2$.

Overall, the same spectral order is required by the combined comparisons in optical and X-ray frequencies, which can be reduced[3] to $\nu_o < \nu_c < \nu_x$. This is feasible for reasonable parameters. The fact that the findings of three independent groups at two distinct observing frequencies can be effortlessly accounted for by both the FS (note the condition on p, though) and the RS qualifies the thick-shell scenario as a very likely explanation for the plateau phase of GRB afterglows.

5 EXAMPLE FITS

In this section, we show two examples of simultaneous fits of physical parameters to optical/IR and X-ray data. We stress that the model uses certain approximations (single zone, thin zone, sharp spectral breaks) that mainly affect the relative flux levels of the FS and the RS. Given those approximations, the fits are performed mostly to show how the overall properties of observations, before and after the injection break, can be explained with the presented model. For that reason we have not attempted a χ^2 minimization to obtain best-fitting values of the physical parameters, but we mostly

[3] Formally speaking, it is also necessary that $\nu_m < \nu_o$, but if this were not the case, optical light curves would rise after the injection break, something never observed.

focus on the duration of the plateau phase and the contribution of the RS.

The two afterglows we fit are of GRB 080928 and GRB 090423. In both cases, the X-ray fluxes come from the *Swift*/XRT GRB light-curve repository (Evans et al. 2007, 2009). For GRB 080928, the optical light curves are taken from Rossi et al. (2011). For GRB 090423, the infrared fluxes are from Tanvir et al. (2009).

5.1 GRB 080928

In Figs 6 and 7, we present data at 10 keV (2.418×10^{18} Hz) and optical bands, respectively, along with model light curves for GRB 080928. Optical data points combine observations in the R (4.55×10^{14} Hz), V (5.48×10^{14} Hz), B (6.83×10^{14} Hz) and U (8.65×10^{14} Hz) bands. The optical light curve is shown for the V band, and all data points from other bands have been shifted to that frequency, using a spectral slope of -1. We interpret the break at $t_{\rm obs} \simeq 10^4$ s as the injection break, which implies $\Delta t = 4 \times 10^3$ s. A jet break around $t_{\rm obs} \simeq 8 \times 10^4$ s implies that the real energy content of the blast wave is $E_{\rm bw} = 1.26 \times 10^{51}$ erg. The contribution of the RS is significant both in optical and X-ray frequencies. The resulting value for p is consistent with the findings of Rossi et al. (2011).

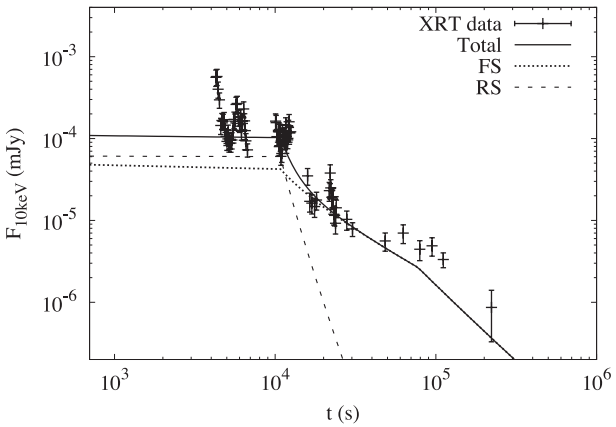

Figure 6. Fit to the X-ray afterglow light curve of GRB 080928. X-ray flux is presented at 10 keV. Physical parameters are $E = 7 \times 10^{52}$ erg, $n_1 = 0.7\,{\rm cm}^{-3}$, $\Delta t = 4 \times 10^3$ s, $\eta = 500$, $q = 0$, $\epsilon_{\rm e} = 0.29$, $\epsilon_{\rm B} = 5.8 \times 10^{-3}$, $p = 2.09$, $\theta_{\rm j} = 11^\circ$, $d = 3.95 \times 10^{28}$ cm and $z = 1.6919$.

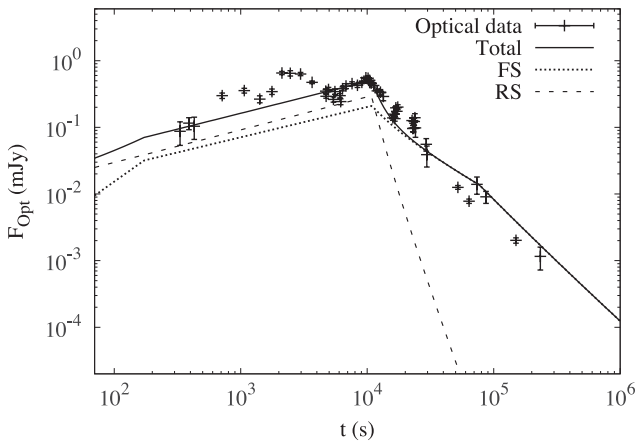

Figure 7. Fit to the optical afterglow light curve of GRB 080928. This figure contains data from the U, B, V and R bands, all shifted to the B band assuming a power-law spectrum with spectral index $\beta_{\rm O} \approx -1$. Physical parameters are as presented in the caption of Fig. 6.

5.2 GRB 090423

In Figs 8 and 9, we present data at 10 keV (2.418×10^{18} Hz) and infrared bands, respectively, along with model light curves for GRB 090423. Infrared data points combine observations in the K (1.38×10^{14} Hz), H (1.82×10^{14} Hz) and J (2.4×10^{14} Hz) bands. The infrared light curve has been calculated for a representative frequency of 1.8×10^{14} Hz. We interpret the break at $t_{\rm obs} \simeq 5 \times 10^4$ s as the injection break. Due to the large redshift of GRB 090423, we find $\Delta t = 4.9 \times 10^3$ s. A jet break at $t_{\rm obs} \simeq 3 \times 10^5$ s is needed to account for the last data point both in the IR and in X-rays. The inferred isotropic energy and jet angle imply that the real energy content of the blast wave is $E_{\rm bw} = 8.8 \times 10^{51}$ erg. The value of q for GRB 090423 is -0.39. Similarly to the case of GRB 080928, the contribution of the RS is substantial both in X-ray and infrared

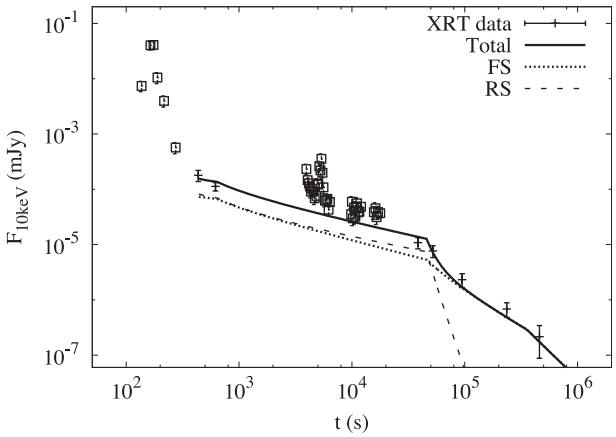

Figure 8. Fit to the X-ray afterglow light curve of GRB 090423. X-ray flux is presented at 10 keV. Data points with squares have been excluded from the fit, as they are a result of high-latitude emission (before 10^3 s) and flaring behaviour (around 10^4 s). Physical parameters are $E = 1.6 \times 10^{54}$ erg, $n_1 = 3.2 \times 10^{-2}\,{\rm cm}^{-3}$, $\Delta t = 5 \times 10^3$ s, $\eta = 400$, $q = -0.39$, $\epsilon_{\rm e} = 0.18$, $\epsilon_{\rm B} = 4.1 \times 10^{-4}$, $p = 2.23$, $\theta_{\rm j} = 6^\circ$, $d = 2.577 \times 10^{29}$ cm and $z = 8.1$.

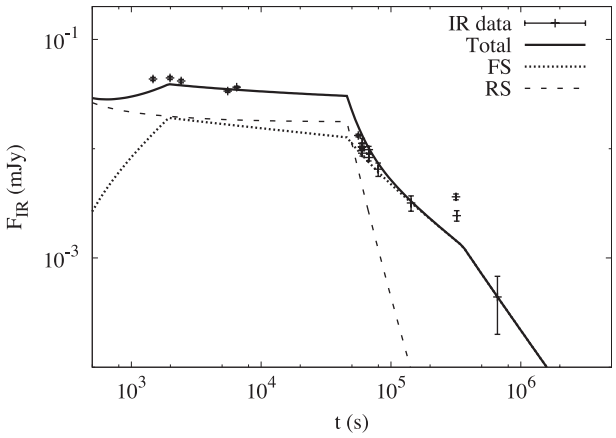

Figure 9. Fit to the IR afterglow light curve of GRB 090423. Data from the K, H and J bands have been used in this figure. Physical parameters are as presented in the caption of Fig. 8.

frequencies, which leads to the characteristic curved shape of the light curves after the injection break.

X-ray observations before 3×10^3 s and around 10^4 s, observer time, have not been fitted. The reason is that both of these periods reveal intense flaring activity superimposed on the baseline flux. These flares probably signal episodic activity of the central engine and cannot be accounted for by the smooth-injection model we are using.

6 DISCUSSION

We have presented simple analytic calculations of blast-wave dynamics in the thick-shell scenario. Based on those, we have shown how the spectra of the FS and the RS can be constructed self-consistently, at any observer time. The combined output of the two regions can account for a big part of the diversity observed in the plateau phase of GRB afterglows, even in the simple case where the FS and the RS share the same microphysics.

6.1 Model assumptions

In the derivation of the presented formulas, several approximations have been made. The most important one is that of a homogeneous layer, both for regions 2 and 3. Kobayashi & Sari (2000) have studied numerically the profile of the blast wave in the thick-shell case and found small deviations from homogeneity. These deviations, however, are expected to have a small impact on the flux levels. Due to the pressure gradient (pressure rises monotonically, but slowly from the RS to the FS), the flux ratio $F_{\rm FS}/F_{\rm RS}$ is probably underestimated in this work. A numerical approach is necessary to assess accurately the relative strength of the two regions.

At a more fundamental level lies the issue of the existence of strong RS in the first place. Doubts arise due to the degree of magnetization of the ejecta, which, if high, is widely expected to hinder the generation of powerful shocks. Matter ejected from the central engines of GRBs carries a significant degree of magnetization in the scenario of magnetically driven ejecta (Komissarov & Barkov 2009), but also in the case of neutrino-driven ejecta (MacFadyen & Woosley 1999). In general, we expect a modification of the magnetization during the interactions that give rise to the prompt emission. However, this modification may be small for radiatively efficient internal shocks (Komissarov 2012). This implies that if at the time the prompt emission is produced the outflow is magnetically dominated, it is likely to remain so. This would lead to a suppression of the RS afterglow emission compared to the flux levels presented in this paper. Conversely, if the magnetic component of the ejecta's energy is not dominant (kinetic-energy-dominated ejecta), a strong RS is expected to form. Mimica, Giannios & Aloy (2010) have numerically studied the influence of the ejecta magnetization on early afterglow spectra and found that radiation from the RS is strongest for a ratio of magnetic to kinetic energy 0.01−0.1. In that case, assuming that the source of the post-shock magnetic field is the shock amplification of pre-existing fields, region 3 is expected to carry a higher fraction of magnetic energy ($\epsilon_{\rm B}$) than region 2, which will make the RS emission even stronger.

6.2 Implications

6.2.1 Shallow decay

Regardless of the uncertainties in the relative flux levels of the FS and the RS, our results for the temporal scalings of the observed flux still hold. These scalings predict a shallow decay or smoothly rising light curves for all optically thin PLS of the synchrotron spectrum, a defining feature of the plateau phase of GRB afterglows. This result is independent of which region (FS or RS) is dominating the radiation.

During the plateau phase, X-ray and optical light curves can be quite different. Even if the FS dominates the emission, chromatic breaks (due to the passage of critical frequencies) and different decay indices between two bands are possible. The range of possibilities widens when RS emission becomes considerable. The injection break can be accompanied by a change of the spectral index in one or more frequencies. Additionally, the behaviour of the light curves after the injection break will be affected by the relative contribution of the RS at the end of the plateau phase, which may be different across the spectrum. Furthermore, if the microphysics of region 3 is different from that of region 2, the picture can become even more complicated. In that scenario, different values of $\epsilon_{\rm B}$ will result in different values of $\nu_{\rm c}$ which may result in additional breaks. Different values of p may lead to varying decay indices and spectral evolution during achromatic breaks.

All of the possibilities mentioned above have been observed (e.g. Panaitescu & Vestrand 2011; Li et al. 2012). Perhaps, the only observed feature of the plateau phase that cannot be explained by the proposed model is the existence of a handful of chromatic breaks that are not accompanied by spectral evolution (e.g. Panaitescu et al. 2006b). The fact that those breaks are chromatic excludes the possibility of them being injection or jet breaks. The constancy of the spectral index excludes the possibility of a critical frequency causing the break. Since these breaks are mostly observed in X-rays, a reasonable suggestion is that they originate from inverse Compton scattering, something which does not exclude the presence of energy injection (see, for example, Panaitescu & Vestrand 2012).

6.2.2 The $F_{\rm b}$−$t_{\rm b}$ relation

Based on scalings for the spectral parameters during the plateau phase, we have derived predictions of the thick-shell scenario for the $F_{\rm b}$−$t_{\rm b}$ relation, both for the FS and the RS. We should stress that these predictions (presented in Table 3) are not sensitive to the main approximations of the model, but derive from basic considerations of the dynamics and the jump conditions at both the FS and the RS. Therefore, they are expected to hold also in a more thorough analysis of the presented physical model.

In Fig. 5, predictions for the $F_{\rm b}$−$t_{\rm b}$ relation are compared against the observationally inferred scalings of Panaitescu & Vestrand (2011) and Li et al. (2012) for optical frequencies. Based on those scalings, we cannot firmly exclude any of the regions 2 or 3 as the origin of optical emission at the time of the injection break. However, the findings of both groups are more easily accommodated by the RS. Especially under the tight constraints of the relation of Li et al. (2012), the FS would require special conditions ($p < 2.2$) across a number of different afterglows to produce the observed scalings. Therefore, we consider emission from the RS to be likely dominant in, at least, a fraction of the observed afterglows. This picture is confirmed when scalings in X-ray frequencies are also taken into account (Dainotti et al. 2013), providing an independent confirmation of the model's agreement with observations, for reasonable physical parameters.

A characteristic feature in RS-dominated light curves is the short-lived steep decay right after the injection break, which is a result of the sudden termination of energy injection. This is seen in some

afterglows, but is absent in others. Based on our analysis we expect the RS to contribute significantly, whatever the physical parameters of the model, as long as the microphysics of regions 2 and 3 are similar. Therefore, we conclude that afterglows that show no observational signature of the RS at the injection break originate from blast waves with very different microphysics parameters between the FS and the RS. The most plausible explanation for this is for the unshocked ejecta to carry a significant degree of magnetization (>0.1), something which would result in suppressed emission from region 3 (Mimica et al. 2010). However, there are examples (like the afterglows fitted in this paper) where emission from the RS is likely to be dominant at the injection break. Consequently, we infer that the outflows that produced these afterglows carried a lower magnetization degree, before being shocked by the RS.

Radiation from the RS has been neglected in most studies so far, at least in the cases where the RS becomes ultrarelativistic before the injection break. This may have important consequences on the inferred values of blast-wave physical parameters through modelling. Our analysis of the physical model and the observed anticorrelation between F_b and t_b demonstrates that the emission of the RS can be important and should be taken into account. A similar conclusion was reached by Uhm & Beloborodov (2007); only in their analysis the RS is responsible for the entire afterglow emission. We propose that the RS emission is significant during the plateau phase of the afterglow, which is typically followed by the 'canonical' afterglow behaviour (Nousek et al. 2006), commonly attributed to the FS. Besides, the majority of afterglows display decay indices compatible with the adiabatic blast-wave model, at sufficiently late times (Racusin et al. 2009).

6.2.3 *Internal shocks and GRB engines*

In the context of internal-shock models for the prompt emission, the observed duration of the GRB roughly corresponds to the lab-frame duration of the central engine (e.g. Sari & Piran 1997). Therefore, the parameter Δt in the thick-shell scenario should also be of the same order. However, there are a few effects that can alter this simplistic picture. We discuss them below.

First of all, the observed duration of the burst, as expressed in T_{90}, is a lower limit to the duration of ejection, since collisions between individual shells (leading to internal shocks) may occur without resulting in significant detections. Secondly, the velocity profile of the ejected matter can be inhomogeneous, causing contraction or expansion of the ejected shell by the time the internal shocks occur (Rees & Meszaros 1998). Furthermore, the collisions of shells during the prompt emission modify the profile of the ejecta, long before the radiation due to external shocks becomes detectable. Mimica, Aloy & Müller (2007) have numerically studied collisions of magnetized shells and find that the post-shock thickness of the ejecta is of similar order to the sum of the widths of the pre-shock shells, with higher magnetization producing thicker ejecta. However, once the internal shocks have crossed the colliding shells, rarefaction waves result in expansion of the ejecta and cooling of the constituent particles.

Under the assumption that the expansion of the post-shock shell (at a velocity of the order of the speed of light) continues until the RS crosses the ejecta, the ratio $t_\mathrm{cr}/\Delta t \sim \Delta t^{-3/4}$ determines the influence of expansion on the width of ejecta that the RS encounters. If $t_\mathrm{cr}/\Delta t < 1$, then that effect is negligible, while if $t_\mathrm{cr}/\Delta t \gg 1$, the ejecta will spread substantially before the RS crosses the entire region, prolonging the duration of energy injection and, therefore, the observed plateau phase. Based on these considerations we conclude that the duration of the plateau phase, reflecting the thickness of the ejecta after the internal shocks, will be at least as long as the prompt emission, while in extreme cases it may last orders of magnitude longer. Similar conclusions hold for the relation between the duration of the plateau phase and the operation of the central engine. Due to the potentially significant expansion of the ejecta after the internal shocks take place, the thick-shell scenario may also be relevant for short bursts with shorter accretion time-scales (Aloy, Janka & Müller 2005) than those of the long-burst progenitors (Woosley 1993).

7 CONCLUSIONS

We have used a simple analytical method to calculate self-consistently synchrotron emission from the FS and the RS in the thick-shell scenario. The approach is generalized to energy injection with arbitrary power, as long as it can be described by a power law in lab-frame time. The resulting light curves exhibit shallow or even inverted temporal decays, the common feature of early afterglow observations. Especially when the contribution of the RS is included, a wide range of possibilities emerge for the behaviour of the light curves during the plateau phase and the injection break. This range includes chromatic and achromatic breaks, widely varying decay indices between different frequencies, injection breaks accompanied by spectral evolution and frequency-dependent behaviour right after the injection break, depending on the relative contribution of the RS at the end of the plateau phase. The picture can become more complex if a different set of microphysics parameters is allowed for the FS and the RS, but also if the jet-break time occurs at time-scales comparable to the injection break, for collimated outflows.

We present formulas for the critical parameters of the spectrum (F_m, ν_m, ν_c) during the plateau phase and for the observed flux in every PLS of the spectrum, both for the FS and the RS. Using the analytical dependence of F_m, ν_m and ν_c on the thickness of the shell ($c\,\Delta t$), we have derived predictions for the $F_\mathrm{b}-t_\mathrm{b}$ relation for all PLS of the FS and the RS. When compared against the observationally inferred relation of Panaitescu & Vestrand (2011) for optical frequencies, the predictions are invariably (for all PLS) in agreement with the observations for the RS, while they are consistent for the FS, as long as $\nu_\mathrm{m} < \nu_\mathrm{o}$. When compared against the much tighter relation of Li et al. (2012), drawn from a bigger sample, emission from the RS is favoured as it satisfies that relation throughout a plausible range of values for p. We consider this strong evidence that the RS may, at least, contribute significantly to the observed flux during the plateau phase in the thick-shell scenario and should therefore be taken into account during modelling. This interpretation is further supported by the results of Dainotti et al. (2013) regarding scalings in X-ray frequencies.

We also present applications of the presented model on two-frequency data sets (X-rays and optical/IR) of GRB 080928 and GRB 090423 that cover the plateau phase, the injection break and the canonical decay of GRB afterglows. The inferred value for Δt is about 5×10^3 s for both bursts, while those of q are approximately 0 and -0.4. For both afterglows, we find that the RS emission at t_b is slightly higher than that of the FS, leading to a characteristic drop in the light curves after the injection break takes place.

ACKNOWLEDGEMENTS

KL would like to thank Dimitrios Giannios for useful discussions. This research was supported by NOVA. RAMJ and AJvdH

acknowledge support from the ERC via Advanced Investigator Grant no. 247295. This work made use of data supplied by the UK Swift Science Data Centre at the University of Leicester.

REFERENCES

Aloy M. A., Janka H.-T., Müller E., 2005, A&A, 436, 273
Beloborodov A. M., Uhm Z. L., 2006, ApJ, 651, L1
Blandford R. D., McKee C. F., 1976, Phys. Fluids, 19, 1130
Chevalier R. A., Li Z.-Y., 2000, ApJ, 536, 195
Curran P. A., Starling R. L. C., van der Horst A. J., Wijers R. A. M. J., 2009, MNRAS, 395, 580
Dai Z. G., Lu T., 1998, A&A, 333, L87
Dainotti M. G., Cardone V. F., Capozziello S., 2008, MNRAS, 391, L79
Dainotti M. G., Petrosian V., Singal J., Ostrowski M., 2013, ApJ, 774, 157
Dall'Osso S., Stratta G., Guetta D., Covino S., De Cesare G., Stella L., 2011, A&A, 526, A121
Evans P. A. et al., 2007, A&A, 469, 379
Evans P. A. et al., 2009, MNRAS, 397, 1177
Gehrels N. et al., 2005, ApJ, 621, 558
Granot J., Loeb A., 2001, ApJ, 551, L63
Granot J., Sari R., 2002, ApJ, 568, 820
Granot J., Miller M., Piran T., Suen W. M., Hughes P. A., 2001, in Costa E., Frontera F., Hjorth J., eds, Gamma-Ray Bursts in the Afterglow Era. Springer-Verlag, Berlin, p. 312
Harrison F. A. et al., 1999, ApJ, 523, L121
Kobayashi S., Sari R., 2000, ApJ, 542, 819
Komissarov S. S., 2012, MNRAS, 422, 326
Komissarov S. S., Barkov M. V., 2009, MNRAS, 397, 1153
Komissarov S. S., Vlahakis N., Königl A., Barkov M. V., 2009, MNRAS, 394, 1182
Kumar P., Panaitescu A., 2003, MNRAS, 346, 905
Li L. et al., 2012, ApJ, 758, 27
MacFadyen A. I., Woosley S. E., 1999, ApJ, 524, 262
Mészáros P., 2006, Rep. Prog. Phys., 69, 2259
Meszaros P., Rees M. J., 1997, ApJ, 476, 232
Mimica P., Aloy M. A., Müller E., 2007, A&A, 466, 93
Mimica P., Giannios D., Aloy M. A., 2010, MNRAS, 407, 2501
Nakar E., Piran T., 2004, MNRAS, 353, 647
Nousek J. A. et al., 2006, ApJ, 642, 389
Panaitescu A., Vestrand W. T., 2011, MNRAS, 414, 3537
Panaitescu A., Vestrand W. T., 2012, MNRAS, 425, 1669
Panaitescu A., Meszaros P., Rees M. J., 1998, ApJ, 503, 314
Panaitescu A., Mészáros P., Gehrels N., Burrows D., Nousek J., 2006a, MNRAS, 366, 1357
Panaitescu A., Mészáros P., Burrows D., Nousek J., Gehrels N., O'Brien P., Willingale R., 2006b, MNRAS, 369, 2059
Racusin J. L. et al., 2009, ApJ, 698, 43
Rees M. J., Meszaros P., 1998, ApJ, 496, L1
Rhoads J. E., 1999, ApJ, 525, 737
Rossi A. et al., 2011, A&A, 529, A142
Rybicki G. B., Lightman A. P., 1986, Radiative Processes in Astrophysics. Wiley, New York
Sari R., Piran T., 1995, ApJ, 455, L143
Sari R., Piran T., 1997, MNRAS, 287, 110
Sari R., Piran T., 1999, ApJ, 520, 641
Sari R., Piran T., Narayan R., 1998, ApJ, 497, L17
Tanvir N. R. et al., 2009, Nature, 461, 1254
Uhm Z. L., 2011, ApJ, 733, 86
Uhm Z. L., Beloborodov A. M., 2007, ApJ, 665, L93
Uhm Z. L., Zhang B., Hascoët R., Daigne F., Mochkovitch R., Park I. H., 2012, ApJ, 761, 147
van Eerten H. J., Zhang W., MacFadyen A., 2010, ApJ, 722, 235
Woosley S. E., 1993, ApJ, 405, 273
Wygoda N., Waxman E., Frail D. A., 2011, ApJ, 738, L23
Zhang W., MacFadyen A., 2009, ApJ, 698, 1261
Zhang B., Fan Y. Z., Dyks J., Kobayashi S., Mészáros P., Burrows D. N., Nousek J. A., Gehrels N., 2006, ApJ, 642, 354

This paper has been typeset from a TEX/LATEX file prepared by the author.